Ultrasound in Med. & Biol., Vol. 41, No. 6, pp. 1651–1667, 2015

0301-5629/$ - see front matter

http://dx.doi.org/10.1016/j.ultrasmedbio.2015.01.028

● *Original Contribution*

EFFECTS OF ULTRASOUND FREQUENCY AND TISSUE STIFFNESS ON THE HISTOTRIPSY INTRINSIC THRESHOLD FOR CAVITATION

Eli Vlaisavljevich,* Kuang-Wei Lin,* Adam Maxwell,† Matthew T. Warnez,‡ Lauren Mancia,‡ Rahul Singh,* Andrew J. Putnam,* Brian Fowlkes,*§ Eric Johnsen,‡ Charles Cain,* and Zhen Xu*¶

*Department of Biomedical Engineering, University of Michigan, Ann Arbor, Michigan, USA; †Department of Urology, University of Washington, Seattle, Washington, USA; ‡Department of Mechanical Engineering, University of Michigan, Ann Arbor, Michigan, USA; §Department of Radiology, University of Michigan, Ann Arbor, Michigan, USA; and ¶Division of Pediatric Cardiology, Department of Pediatrics and Communicable Diseases, University of Michigan, Ann Arbor, Michigan, USA

(*Received* 24 *September* 2014; *revised* 26 *January* 2015; *in final form* 26 *January* 2015)

Abstract—Histotripsy is an ultrasound ablation method that depends on the initiation of a cavitation bubble cloud to fractionate soft tissue. Previous work has indicated that a cavitation cloud can be formed by a single pulse with one high-amplitude negative cycle, when the negative pressure amplitude directly exceeds a pressure threshold intrinsic to the medium. We hypothesize that the intrinsic threshold in water-based tissues is determined by the properties of the water inside the tissue, and changes in tissue stiffness or ultrasound frequency will have a minimal impact on the histotripsy intrinsic threshold. To test this hypothesis, the histotripsy intrinsic threshold was investigated both experimentally and theoretically. The probability of cavitation was measured by subjecting tissue phantoms with adjustable mechanical properties and *ex vivo* tissues to a histotripsy pulse of 1–2 cycles produced by 345-kHz, 500-kHz, 1.5-MHz and 3-MHz histotripsy transducers. Cavitation was detected and characterized by passive cavitation detection and high-speed photography, from which the probability of cavitation was measured versus pressure amplitude. The results revealed that the intrinsic threshold (the negative pressure at which probability = 0.5) is independent of stiffness for Young's moduli (E) <1 MPa, with only a small increase (~2–3 MPa) in the intrinsic threshold for tendon (E = 380 MPa). Additionally, results for all samples revealed only a small increase of ~2–3 MPa when the frequency was increased from 345 kHz to 3 MHz. The intrinsic threshold was measured to be between 24.7 and 30.6 MPa for all samples and frequencies tested in this study. Overall, the results of this study indicate that the intrinsic threshold to initiate a histotripsy bubble cloud is not significantly affected by tissue stiffness or ultrasound frequency in the hundreds of kilohertz to megahertz range. (E-mail: Evlaisav@umich.edu)

Key Words: **Histotripsy, Cavitation, Intrinsic threshold, Frequency, Tissue mechanical properties.**

INTRODUCTION

Histotripsy is a non-invasive tissue ablation method that controllably fractionates soft tissue through cavitation generated by high-pressure (>10 MPa), short-duration (<20 μs) ultrasound pulses at low duty cycles (<1%) (Parsons et al. 2006a; Roberts et al. 2006; Xu et al. 2005). Histotripsy depends on the initiation and maintenance of a dense cavitation bubble cloud to produce mechanical tissue fractionation (Parsons et al. 2007; Xu et al. 2005). With sufficiently high pressure and dose, histotripsy can completely fractionate soft tissue into an acellular liquid homogenate, resulting in effective tissue disintegration (Hall et al. 2007; Xu et al. 2005).

It has been reported that there are two mechanisms by which a histotripsy cavitation cloud can be generated. In the first, the "shock scattering mechanism," a dense bubble cloud is formed from a single multicycle histotripsy pulse (*e.g.,* 3–20 cycles) using shock scattering from sparse initial bubbles formed and expanded during the initial cycles of the pulse (Maxwell et al. 2011b). In this process, single or sparse initial bubbles, which for the purpose of this study are termed *incidental bubbles*,

Address correspondence to: Eli Vlaisavljevich, Department of Biomedical Engineering, University of Michigan, 2200 Bonisteel Boulevard, Ann Arbor, MI 48109, USA. E-mail: Evlaisav@umich.edu

Conflicts of interest: Charles Cain, J. Brian Fowlkes and Zhen Xu have financial interests and/or other relationships with HistoSonics Inc.

are formed from large heterogeneous nuclei in the focus or as the result of the growth of cavitation nuclei over multiple cycles (Maxwell et al. 2010, 2011a). These incidental bubbles are formed significantly below the intrinsic threshold, which is defined as the threshold to generate cavitation directly from the incident negative pressure phase of a single-cycle pulse. These incidental bubbles act as pressure release surfaces wherein the following positive pressure shock fronts are inverted and superimposed on the incident negative pressure phase to form negative pressures that produce a dense cavitation cloud growing back toward the transducer (Maxwell et al. 2011b). By the shock scattering mechanism, bubble clouds are initiated at negative pressures ranging from 10 to 28 MPa. Because of the complexity of the shock scattering process, multiple factors determine whether a cloud is initiated, including the distribution of heterogeneous nuclei in the focal region, the size and shape of initial single bubbles, the number of cycles, the shock rise time and the positive-pressure amplitudes (Maxwell et al. 2010, 2011b; Vlaisavljevich et al. 2014b; Xu et al. 2007). Additionally, our previous study reported that increases in tissue stiffness result in higher cloud initiation thresholds when using the shock scattering mechanism of bubble cloud formation (Vlaisavljevich et al. 2014b). The mechanism responsible for this increase was hypothesized to be decreased bubble expansion in tissues with higher Young's modulus, which leads to reduced shock scattering (Vlaisavljevich et al. 2014b). Results of that study suggested that bubble cloud formation in tissues with Young's moduli >100 kPa was driven primarily by the negative pressure of the incident wave, whereas the contributions of shock scattering were significantly decreased because of suppressed bubble expansion (Vlaisavljevich et al. 2014b).

In addition to the shock scattering mechanism, which uses a multicycle ultrasound pulse, there is the "intrinsic threshold mechanism," in which a 1- to 2-cycle pulse with a single dominant negative-pressure phase is used to generate a bubble cloud directly from the negative pressure of the incident wave (Lin et al. 2014c; Maxwell et al. 2013). With these short pulses, cavitation initiation depends solely on the negative pressure when it exceeds a distinct threshold intrinsic to the medium, without the contributions from shock scattering, resulting in a bubble cloud matching the portion of the focal region above the intrinsic threshold (Lin et al. 2014c; Maxwell et al. 2013). In contrast to shock scattering, it is possible that the histotripsy intrinsic threshold will not be affected by changes in tissue stiffness, because the intrinsic threshold mechanism of cloud initiation does not rely on the expansion of initial incidental bubbles to initiate a dense bubble cloud. In the previous study by Maxwell et al. (2013), an intrinsic threshold of approximately 26–30 MPa was observed for water-based soft tissues and tissue phantoms using a 1.1-MHz histotripsy transducer, whereas the threshold for tissue composed primarily of lipids was significantly lower (15.4 MPa for adipose tissue). However, Maxwell et al. (2013) were limited to measurement of the cavitation probability at a single ultrasound frequency (1.1 MHz) and in tissue phantoms and soft tissues with a limited range of Young's moduli (≤36 kPa).

In this study, we investigate the effects of tissue stiffness and ultrasound frequency on the histotripsy intrinsic threshold in tissues with a wide range of Young's moduli using multiple frequencies. To accomplish this goal, the probability of inertial cavitation was measured by subjecting water, mechanically tunable agarose tissue phantoms and various *ex vivo* tissues covering a wide range of stiffness (Young's moduli = 1.13 kPa–380 MPa) to histotripsy pulses produced by 345-kHz, 500-kHz, 1.5-MHz, and 3-MHz histotripsy transducers. The intrinsic threshold was defined as the peak negative pressure at which the probability of generating cavitation, p_{cav}, from a single histotripsy pulse was $p_{cav} = 0.5$. As previous studies have indicated that there is a significant difference in the intrinsic threshold between water-based tissues and lipid-based tissues, and because the former type covers most soft tissues, we focused on water-based tissues in this study. The results of this study will help explain the role of ultrasound frequency and tissue stiffness in generating a histotripsy bubble cloud using the intrinsic threshold method.

In the final part of this study, two numerical models are used to investigate the potential characteristics of the "intrinsic nuclei" in tissue. Maxwell et al. (2013) suggested that the histotripsy intrinsic threshold relies on cavitation nuclei that are intrinsic to the tissue. By *intrinsic*, we mean that the nuclei appear to be associated with the properties of the medium itself rather than impurities. Although it is possible that these nuclei too are related to impurities, it seems unlikely, as several groups using different sample processing methods have measured approximately the same threshold for inertial cavitation associated with these nuclei in the range 24 to 33 MPa in distilled water (Briggs 1950; Caupin and Herbert 2006; Greenspan and Tschiegg 1982; Herbert et al. 2006; Maxwell et al. 2013; Sankin and Teslenko 2003). Various theoretical studies suggest that the intrinsic nuclei can be modeled as semipermanent stabilized gas nuclei caused by impurities in the liquid (Bunkin et al. 2009; Harvey et al. 1944; Sankin and Teslenko 2003; Yount 1979) or spontaneous nuclei that form bubbles in a medium by energy-density fluctuations described by classic nucleation theory (Arvengas et al. 2011a, 2011b; Fisher 1948; Pettersen et al. 1994). In

the previous study by Maxwell et al. (2013), a theoretical simulation using 2.5-nm stabilized nuclei resulted in a cavitation threshold closely matching experiments. However, it remains unclear if the intrinsic nuclei are small, stabilized gas nuclei or spontaneous nuclei. Therefore, in this study, two separate simulations were performed to investigate the pressure thresholds predicted by spontaneous and nanometer-sized stable nuclei, with the intention of providing a theoretical explanation for the intrinsic thresholds measured experimentally.

METHODS

Sample preparation

The intrinsic cavitation threshold was tested for distilled water, mechanically tunable agarose tissue phantoms and *ex vivo* bovine tissues (liver, tongue, and tendon). The agarose tissue phantoms and *ex vivo* tissues selected are all water based, as this study focused on water-based tissue. Cavitation probability versus pressure was measured in three samples of each type.

First, the effect of ultrasound frequency on the cavitation threshold was tested in distilled, degassed water (15% O_2). Water was degassed before experiments to minimize any stable gas bubbles in the sample. Water samples were degassed by repeatedly boiling them and then letting the samples cool under a partial vacuum (~20 kPa, absolute) for 30 min. For comparison, the threshold in minimally degassed water (90% O_2), was also investigated. Gas saturation was measured using an O_2 meter (DO200, YSI, Yellow Springs, OH, USA).

To compare the effects of tissue stiffness on the cavitation threshold, mechanically tunable agarose tissue phantoms were used to provide a well-controlled elastic medium for this study. Agarose phantoms were selected to cover the mechanical stiffness of tissues found in the body, from non-load-bearing tissues such as lung, liver, and kidney (Young's moduli ranging from 1 to 10 kPa) to strong load-bearing tissues such as cartilage (Young's moduli of ~1 MPa). Agarose phantoms of 0.3%, 1%, 2.5% and 5% w/v were prepared by slowly mixing agarose powder (Agarose Type VII, Sigma-Aldrich, St. Louis, MO, USA) into saline solution (0.9% sodium chloride, Hospira, Lake Forest, IL, USA) heated to boiling temperature. The solution was stirred on a hot plate until the gel became completely transparent and then allowed to boil for 10 min. After boiling, solutions were allowed to cool and were degassed under a partial vacuum (~20 kPa, absolute) for 30 min. After degassing, the solution was poured into tissue phantom holders and placed in a refrigerator at 4°C to allow the agarose solution to solidify before use. The mechanical properties of the agarose phantoms were measured using a parallel-plate AR-G2 rheometer (TA Instruments, New Castle, DE, USA) on a Peltier stage, similar to previous studies (Balgude et al. 2001; Ulrich et al. 2010). The stage was initially heated to 90°C, and samples were allowed to melt for 1 min before the top plate was lowered to create a gap of 1,000 μm. The stage was cooled to 60°C, excess solution was wiped off and the gap was sealed with mineral oil (Sigma-Aldrich) to prevent evaporation. Samples were held at 60°C for 2 min to ensure a uniform starting temperature and then cured at 4°C for 20 min. The samples were then heated to 20°C for 10 min, and the mechanical properties were measured. Shear modulus (G) was measured at a frequency of 0.1 radian/s, with 0.05% strain for 5% and 2.5% tissue phantoms and 0.1% strain for 1% and 0.3% tissue phantoms. Three independent samples were measured for each weight percentage, with the results reported as the mean ± a 95% confidence interval. The Young's modulus (E) was estimated from the shear modulus as $E = 3G$ (Table 1).

For *ex vivo* tissue experiments, fresh bovine liver, tongue, and tendon were excised at a local slaughterhouse, immediately placed into degassed 0.9% saline solution and stored at 4°C until experiments. Tissue samples were sectioned and warmed to room temperature in degassed saline under a partial vacuum (~20 kPa, absolute) for 4 h before experiments. Each sample was embedded in a 1% agarose tissue phantom, which was prepared as described above. The samples were embedded in agarose to fix the position of the tissue and displace any remaining air. All tissue samples were several centimeters in the dimension transverse to the acoustic axis and at least 1 cm in dimension along the acoustic axis as positioned during testing. All tissues were used within 48 h of harvesting. To compare the cavitation threshold results with tissue stiffness, Young's modulus values from the literature were chosen as a tissue mechanical property metric for this study and are provided in Table 1 (Diem and Lentner 1970; Duck 1990;

Table 1. Sample mechanical properties for all samples tested in this study*

	Young's modulus (kPa)	Density (kg/m^3)	Water content (%)
Water	—	998	100
0.3% Agarose	1.13 ± 0.47	1,003.0	98.8
1% Agarose	21.7 ± 1.0	1,010.0	98.1
2.5% Agarose	242 ± 27	1,025.0	96.7
5% Agarose	570 ± 46	1,050.0	94.3
Liver	8.7	1,060	74.2
Tongue	25	—	66
Tendon	380,000	1,165	63

* The Young's modulus of agarose tissue phantoms was measured using shear rheology (E = 3 G). *Ex vivo* bovine liver, tongue and tendon were used to cover a large range of tissue Young's modulus as measured in the literature (Diem and Lentner 1970; Duck 1990; ICRP 1975; ICRU 1989; Staubli et al. 1999; Woodard and White 1986; Yamada 1973).

International Commission on Radiological Protection [ICRP] 1975; International Commission on Radiological Units [ICRU] 1989; Staubli et al. 1999; Woodard and White 1986; Yamada 1973).

Histotripsy pulse generation

Histotripsy pulses were generated at four ultrasound frequencies (345 kHz, 500 kHz, 1.5 MHz and 3 MHz) using three custom-built histotripsy transducers. The 345-kHz pulses were generated by a 20-element array transducer with a geometric focus of 150 mm, an aperture size of 272 mm and an *f*-number of 0.55. The 1.5-MHz pulses were generated by a 6-element array transducer with a geometric focus of 55 mm, an aperture of 79 mm in the elevational direction and 69 mm in the lateral direction and effective f-numbers of 0.7 and 0.8 in the elevational and lateral directions, respectively. The 500-kHz and 3-MHz pulses were generated by a dual-frequency array transducer that consisted of twelve 500-kHz elements and seven 3-MHz elements. For the 500-kHz elements, the geometric focus was 40 mm, the aperture size was 71 mm and the *f*-number was 0.56. For the 3-MHz elements, the geometric focus was 40 mm, the aperture size was 80 mm and the *f*-number was 0.5. The design of this dual-frequency transducer was described in detail in a previous study (Lin et al. 2014a).

To measure the intrinsic threshold in each sample, short pulses with a single dominant negative-pressure phase were applied to the sample (Fig. 1). We expect that the differences in the *f*-numbers of the transducers do not affect the intrinsic threshold measurements, as the intrinsic threshold depends primarily on the negative-pressure phase of the pulse and is not affected by the positive-pressure phase or non-linear propagation, although it may be affected by differences in the beam dimensions (Lin et al. 2014b, 2014c; Maxwell et al. 2013). To generate a short therapy pulse, a custom high-voltage pulser developed in-house was used to drive the transducers. The pulser was connected to a field-programmable gate array development board (Altera DE1 Terasic Technology, Dover, DE, USA) specifically programmed for histotripsy therapy pulsing. This setup allowed the transducers to output short pulses consisting of fewer than two cycles. A fiberoptic probe hydrophone built in-house (Parsons et al. 2006b) was used to measure the acoustic output pressure of the transducers. At higher pressure levels, the acoustic output could not be directly measured because of cavitation at the fiber tip. These pressures were estimated by a summation of the output focal p_- values from individual transducer elements. This approximation assumes that minimal non-linear distortion of the waveform occurs within the focal region. In a previous study (Maxwell et al. 2013), this estimated p_- was found to be accurate within 15% compared with direct focal pressure measurements in water and in a medium with a higher cavitation threshold, 1,3-butanediol.

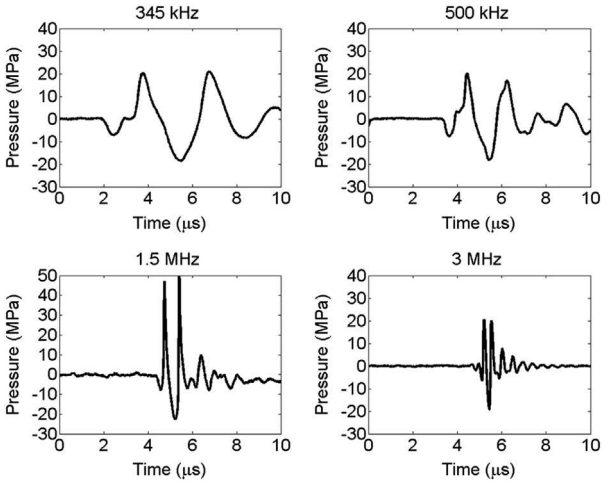

Fig. 1. Plots of example histotripsy waveforms produced by 345-kHz, 500-kHz, 1.5-MHz and 3-MHz histotripsy transducers.

For threshold experiments, histotripsy pulses were applied inside different samples at a pulse repetition frequency (PRF) of 0.5 Hz. The PRF was kept very low to minimize the possibility that cavitation from one pulse would change the probability of cavitation on a subsequent pulse. A previous study (Maxwell et al. 2013) had reported that for PRFs >1 Hz, cavitation during a pulse increased the likelihood of cavitation on a subsequent pulse, but this effect was not observed for PRFs <1 Hz, as the residual nuclei from a histotripsy pulse dissolve within ~1 s after the histotripsy pulse. In solid samples, the focus was translated for each pulse by 1 mm transverse to the acoustic propagation direction in a 10 × 10 grid for each pressure level to minimize the effects of cavitation damage to the solid sample altering the probability of cavitation. Although each focal volume only received a single pulse for solid samples, the PRF was kept at a low rate of 0.5 Hz for consistency. Translating the volume and using a low PRF were both done to prevent the effects of the previous pulse from affecting the results on a subsequent pulse. At each pressure level tested, 100 pulses were applied to the sample.

Cavitation detection using optical imaging

High-speed optical imaging was used to detect cavitation for water and agarose tissue phantoms using two high-speed cameras (Fig. 2). The cameras were triggered to record one image for each applied pulse at a time point approximately corresponding to the maximum bubble expansion for each sample and frequency combination. These time points were determined before experiments in a separate study by changing the delay time on the

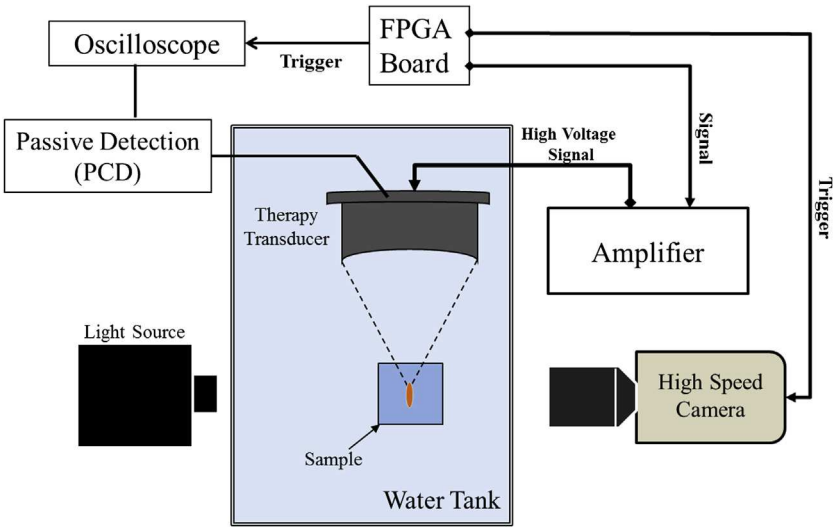

Fig. 2. Experimental setup. Histotripsy pulses were applied to the inside of water, mechanically tunable tissue phantoms and various *ex vivo* bovine tissues. Cavitation was monitored using high-speed optical imaging for transparent samples. Additionally, cavitation was monitored using one of the therapy transducer elements as passive cavitation detection (PCD) for all samples. FPGA = field programmable gate array.

camera to reconstruct representative radius-versus-time curves of the bubbles and identify the time corresponding to maximum bubble expansion (Vlaisavljevich et al. 2015. For experiments with the 345-kHz and 1.5-MHz transducers, a high-speed, 1-megapixel CCD camera (Phantom V210, Vision Research, Wayne, NJ, USA) was aligned with the transducer and backlit by a continuous white-light source. The camera was focused using a macro-bellows lens (Tominon 1:4.5, F = 105 mm; Kyocera, Kyoto, Japan), giving the captured images a resolution of approximately 5.9 μm per pixel and 3.4 μm per pixel for 345 kHz and 1.5 MHz, respectively. For experiments with the 500-kHz and 3-MHz dual-frequency transducers, a digital, 1.3-megapixel CCD camera (PN: FL3-U3-13 Y3 M-C, Flea 3; PointGrey, Richmond, BC, Canada) was positioned perpendicularly to the dual-frequency array transducer facing one of its optical windows. A Nikon 4× objective (MRP70040, Nikon, Chiyoda, Tokyo, Japan) was attached to the camera with extension tubes to magnify the image plane, giving the captured images a resolution of approximately 2.5 μm per pixel. A pulsed white-light LED was placed on the diametrically opposed optical window of the dual-frequency array transducer, which provided back-lit illumination. The camera exposure time was 2 μs for all images. After acquisition, shadowgraph images were converted from gray scale to binary by an intensity threshold determined by the background intensity using image processing software (MATLAB, The MathWorks, Natick, MA, USA). Bubbles were indicated as any black regions >5 pixels in diameter. By this criterion, the minimum resolvable bubble radius was 14.75, 6.25, 8.5 and 6.25 μm for the 345-kHz, 500-kHz, 1.5-MHz and 3-MHz transducers, respectively. The number of frames that contained cavitation bubbles was recorded, and the fraction of total frames (out of 100) for which any cavitation was detected was determined as the cavitation probability.

Passive cavitation detection

High-speed imaging simplifies the detection of cavitation in transparent media, but could not be used with tissue samples. As a result, an acoustic method was also used to identify cavitation in the focal zone in all media. Additionally, because relying on an image of the bubbles taken at a single time point is a potential limitation, the passive cavitation detection (PCD) method allowed cavitation to be monitored over a much longer period after the passage of the pulse. For each experiment, one of the transducer's therapy elements was also used for PCD to detect the presence of cavitation in the focal region (Fig. 2). The PCD signal was connected to an oscilloscope (LT372, Lecroy, Chestnut Ridge, NY, USA), with the time window selected to record the backscattering of the therapy pulse from cavitation bubbles (Herbert et al. 2006; Maxwell et al. 2013; Roy et al. 1990). To determine whether cavitation occurred during a pulse, the signal generated by backscattering of the incident pulse from the focus was analyzed with the method used by Maxwell et al. (2013). In this process, a bubble is generated by the negative-pressure phase of the pulse, and the subsequent positive pressure is then scattered off the bubble and detected by the PCD. It should, however, be noted that subsequent bubbles are not formed from shock scattering in this case because the pulse contains a single dominant negative

phase. Previous work had indicated that generating a bubble cloud from shock scattering requires both the scattering of the positive pressure and the constructive interference with the subsequent negative cycles to generate bubbles (Maxwell et al. 2010, 2011b; Vlaisavljevich et al. 2014b). Although some positive pressure is scattered here, there are no (or very small) subsequent negative-pressure cycles to constructively interfere with the scattered shockwave. The exception to this would be if the reflected shock directly exceeds the intrinsic threshold, which would not be expected (and was not observed) under the conditions used in this study. The backscattered pressure amplitude was received by the PCD at the time point corresponding to two times the time of flight for the focal length of the respective transducers. The integrated frequency power spectrum (S_{PCD}) of the backscatter signal was used as a measure of whether cavitation occurred according to the method previously described by Maxwell et al. (2013).

Intrinsic threshold measurement and comparison

The probability of observing cavitation followed a sigmoid function, given by

$$P(p_-) = \frac{1}{2} + \mathrm{erf}\left(\frac{p_- - p_{int}}{\sqrt{2\sigma^2}}\right) \quad (1)$$

where erf is the error function, p_{int} is the negative pressure at which the probability $p_{cav} = 0.5$ and σ is a variable related to the width of the transition between $p_{cav} = 0$ and $p_{cav} = 1$, with $\pm\sigma$ giving the difference in pressure from about $p_{cav} = 0.15$ to $p_{cav} = 0.85$ for the fit (Maxwell et al. 2013). The intrinsic threshold for each sample, p_{int}, is defined as the p_- corresponding to $p_{cav} = 0.5$ as calculated by the curve fit. Curve fitting for all data sets was performed using an OriginLab curve-fitting program (OriginPro 9.1, OriginLab, Northampton, MA, USA). The fit curves for all samples were analyzed statistically to determine whether the differences in the p_{int} values were significantly different from each other. The standard errors for p_{int} were estimated by a covariance matrix using the delta method (Hosmer and Lemeshow 1992). The curves were compared using a two-sample t-test with statistic $t(p_{int1} - p_{int2}, \sqrt{SE_1^2 + SE_2^2})$ at a 95% confidence interval. Results were considered statistically significant at $p < 0.05$. Note that the standard error does not include the uncertainty in absolute pressure from the hydrophone measurement, only the uncertainty in the fit, because the p_{int} values are relative.

Threshold simulation: Stabilized nuclei

To provide a theoretical explanation of the experimental results, a numerical model based on a linear Kelvin–Voigt model was used to investigate the effects of tissue stiffness and ultrasound frequency on the pressure threshold, assuming that the intrinsic threshold is due to nanometer-sized stabilized cavitation nuclei in the tissue. In a previous study, a similar model had a pressure threshold matching the histotripsy intrinsic threshold at 1.1 MHz when an initial bubble radius of 2.5 nm was used, corresponding to a threshold for inertial cavitation of 28.1 MPa (Maxwell et al. 2013). For nuclei of this size, surface tension dominates the cavitation threshold, similar to the Blake threshold (Blake 1949; Leighton 1994; Maxwell et al. 2013). To test the effects of tissue stiffness and ultrasound frequency on the threshold for generating inertial cavitation, simulations exposed a 2.5-nm initial bubble to a single peak negative pressure

$$p_a(t) = \begin{cases} p_A\left(\dfrac{1+\cos[\omega(t-\delta)]}{2}\right)^n, & |t-\delta| \le \dfrac{\pi}{\omega} \\ 0, & |t-\delta| > \dfrac{\pi}{\omega} \end{cases} \quad (2)$$

where p_A is the peak negative pressure, ω is the angular frequency of the experimental ultrasound wave, δ is a time delay and n is a curve-fitting parameter, which was set to 3.7 so that the shape of the simulated waveform p_- closely matched the shape and duration of the p_- from the histotripsy waveforms used experimentally. It should be noted that these theoretical waveforms were used for simulations instead of the experimentally measured waveforms (Fig. 1). The positive pressure of the experimentally measured waveforms caused rapid collapse of the bubbles that did not match experiments. One explanation for the mismatch is that the bubble scattered the positive portion of the waveform without shrinking. Although this is a limitation of the current model, it is likely an appropriate assumption considering previous work indicating that the bubbles formed using the intrinsic threshold method are generated directly from the negative pressure of the incident wave and do not depend on the positive pressure (Lin et al. 2014b, 2014c; Maxwell et al. 2013).

For this study, we assumed that the surrounding medium had homogeneous properties and that the bubble contained air and remained spherical. These assumptions allowed us to use a numerical model developed in-house for simulating spherical bubble dynamics in a viscoelastic medium with viscous, elastic, relaxation and retardation effects, including liquid compressibility and heat transfer. Because the present focus is on the initial threshold behavior and the resulting growth, we neglect heat transfer and consider a simple viscoelastic model (linear Kelvin–Voigt) that includes viscosity and elasticity (Yang and Church 2005). In the Kelvin–Voigt model,

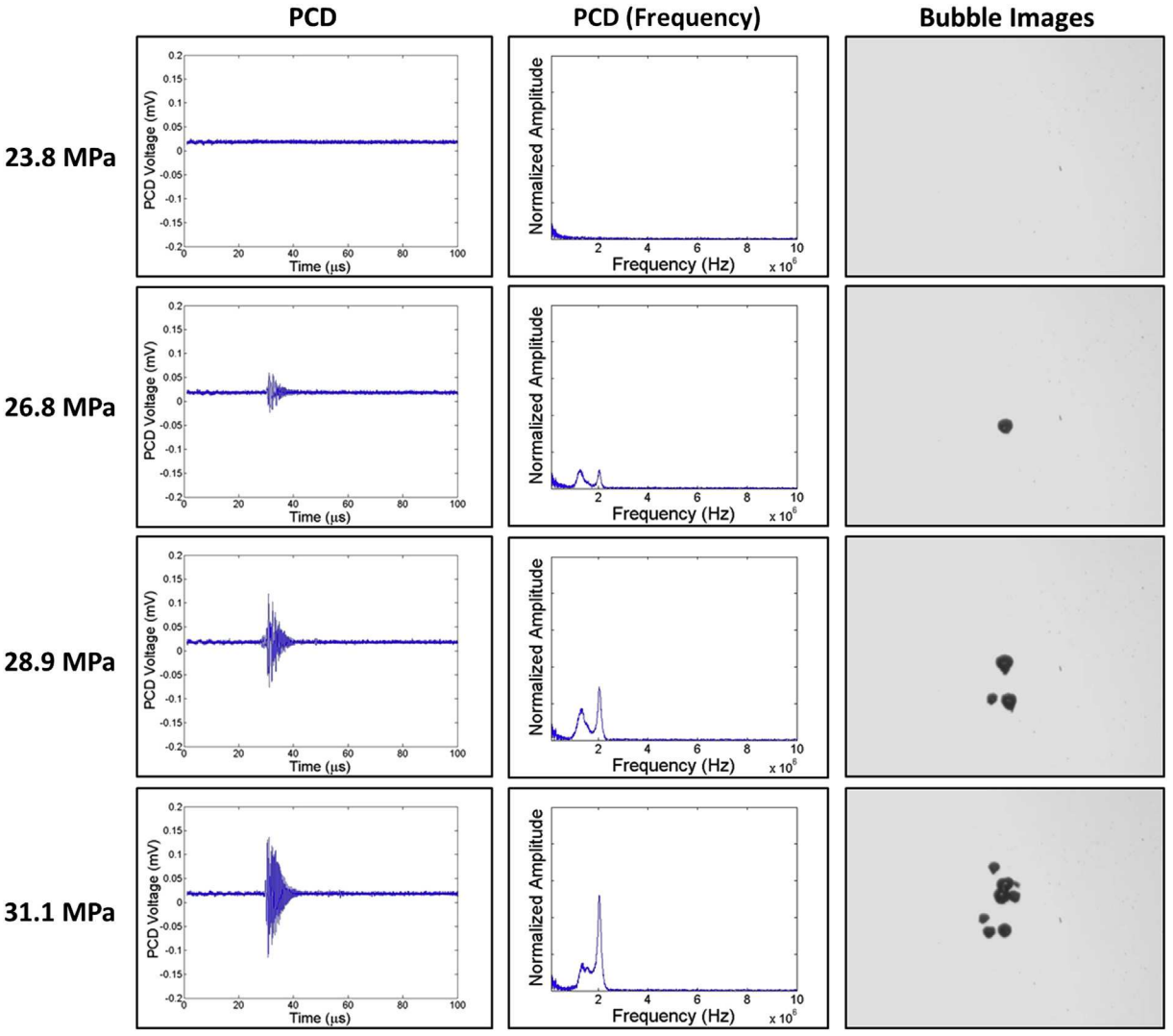

Fig. 3. Cavitation detection. Sample passive cavitation detection (PCD) temporal (left) and frequency (center) signals were used for cavitation detection. Results revealed agreement with high-speed optical images of cavitation (right). Representative images are from 1.5-MHz histotripsy pulses applied to degassed water (ultrasound propagating top to bottom).

the stress tensor τ is related to the deformation tensor γ and the rate of deformation tensor $\dot{\gamma}$ through

$$\tau = 2G\gamma + 2\mu\dot{\gamma} \tag{3}$$

where G is the shear modulus (elasticity), and μ is the viscosity. The stress tensor is related to the bubble radius R through the Keller–Miksis equation (Keller and Miksis 1980)

$$\left(1-\frac{\dot{R}}{c}\right)R\ddot{R}+\frac{3}{2}\left(1-\frac{\dot{R}}{3c}\right)\dot{R}^2=\frac{1}{\rho}\left(1+\frac{\dot{R}}{c}+\frac{R}{c}\frac{d}{dt}\right)\left(p_g-\frac{2S}{R}-p_\infty(t)+3\int_R^\infty\frac{\tau_{rr}}{r}dr\right) \tag{4}$$

which depends on the medium's sound speed, c, density, ρ, and surface tension against air, S. Here $p_\infty(t)$ is the absolute forcing pressure, r is the radial coordinate and overdots denote derivatives with respect to time, t. The air within the bubble is assumed to have spatially uniform pressure given by the polytropic relationship

$$p_g = p_0\left(\frac{R_0}{R}\right)^{3\kappa} \tag{5}$$

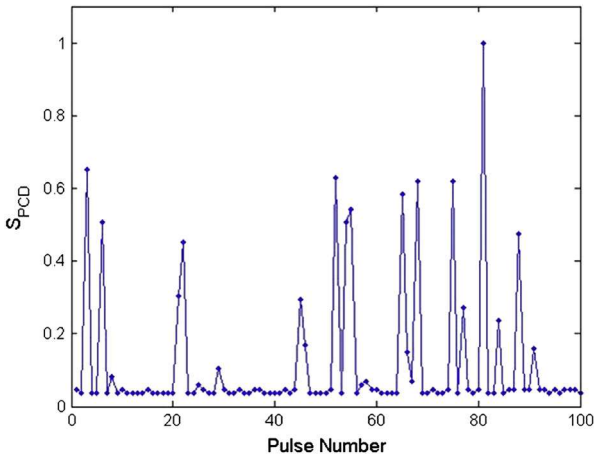

Fig. 4. Example integrated power spectrum (S_{PCD}) bimodal distribution. Results indicate the S_{PCD} for 100 histotripsy pulses applied by the 1.5-MHz transducer at a peak negative pressure of 25.3 MPa. A bimodal distribution is evident, with the lower, more consistent values indicating the absence of cavitation, and the larger, more variable values indicating the presence of one or more bubbles.

where $\kappa = 1.4$ is the ratio of specific heats for air, R_0 is the initial bubble radius and $p_0 = p_\infty(0) + 2S/R_0$ is the initial bubble pressure. Using the Yang and Church model

$$3\int_R^\infty \frac{\tau_{rr}}{r}dr = -\frac{4G}{3}\left(1-\frac{R_0^3}{R^3}\right) - \frac{4\mu\dot{R}}{R} \qquad (6)$$

the Keller–Miksis equation can be solved for the bubble wall acceleration $\ddot{R}$ and integrated in time (Yang and Church 2005). The properties $\rho = 1000$ kg/m^3, $c = 1497$ m/s^2, $\mu = 1.00$ mPa-s (viscosity of water) and $S = 72$ mN-m (water–air surface tension) were used to approximate the surrounding medium. The Young's modulus (approximated for soft tissue as $E = 3G$) was varied in decades from 1 kPa to 10 MPa to compare the effects of Young's modulus on the cavitation threshold. Ultrasound frequencies were 345 kHz, 500 kHz, 1.5 MHz and 3 MHz for comparison with experimental results. The maximum bubble radius was plotted as a function of the peak negative pressure using different ultrasound frequencies and tissue Young's moduli for initial bubble nuclei of 2.5 nm. A further simulation was conducted to investigate the threshold as a function of initial nuclei size to determine the range of nuclei corresponding to the experimentally measured thresholds. The pressure threshold for this simulation was defined as the pressure required to expand an initial bubble to >15 μm in radius, to be consistent with the minimum resolution for optical images recorded experimentally. This criterion is more reasonable for histotripsy therapy than the criteria commonly used for inertial cavitation of $R_{max} > 2R_0$, as previous work has indicated that histotripsy bubbles must be sufficiently expanded to sizes much greater than $2R_0$, often >50 μm, to fractionate tissue (Parsons et al. 2006a; Vlaisavljevich et al. 2013a, 2015; Xu et al. 2007).

Threshold simulation: Spontaneous nucleation

To investigate the effects of ultrasound frequency on the cavitation threshold predicted for spontaneous nucleation, a theoretical analysis was performed based on classic nucleation theory (CNT) (Arvengas et al. 2011a; Caupin and Herbert 2006; Herbert et al. 2006; Pettersen et al. 1994). Previous studies using CNT have suggested that the cavitation threshold decreases at lower frequency because of the larger focal volume and increased duration of the applied p_- (Arvengas et al. 2011a; Pettersen et al. 1994). The threshold predicted by CNT, p_{t_CNT}, was calculated as

$$p_{t\_CNT} = \left(\frac{16\pi\alpha^3}{3k_bT * \ln\frac{\Gamma_0 V_f \tau_f}{\ln 2}}\right)^{0.5} \qquad (7)$$

where α is the surface energy, k_b is Boltzmann's constant, T is temperature in Kelvin, Γ_0 is a pre-factor, V_f is the focal volume for a given frequency and τ_f is the time the focal volume is above a given pressure (Arvengas et al. 2011a, 2011b; Fisher 1948; Herbert et al. 2006; Pettersen et al. 1994). Γ_0 was set to $\Gamma_0 = 10^{33}$ similar to previous work (Pettersen et al. 1994), and T was set to 293 K to match experiments. V_f and τ_f were modified for each frequency, with τ_f set to one-fourth of the acoustic period and V_f representing the focal volume of each transducer. The values of V_f were calculated from the -6-dB full width at half-maximum beam profiles of the transducers used in this study, assuming an ellipsoidal focus, and were 47.07, 7.89, 2.30 and 0.072 mm^3 for 345 kHz, 500 kHz, 1.5 MHz and 3 MHz, respectively. The surface energy α was set to 18.8 mN/m, ~25% of the macroscopic surface tension of water. This value for surface energy was chosen such that results matched the experimental threshold at 500 kHz. Previous work has suggested that because the cavitation nucleus has a nanoscopic size, it is not accurate to use the bulk, macroscopic surface tension value for surface energy (Arvengas et al. 2011b; Herbert et al. 2006). The surface energy value used in this study closely matches the value calculated in a previous study by Herbert et al. (2006) and resulted in more reasonable results for p_{t_CNT} than those calculated using the macroscopic values of surface tension.

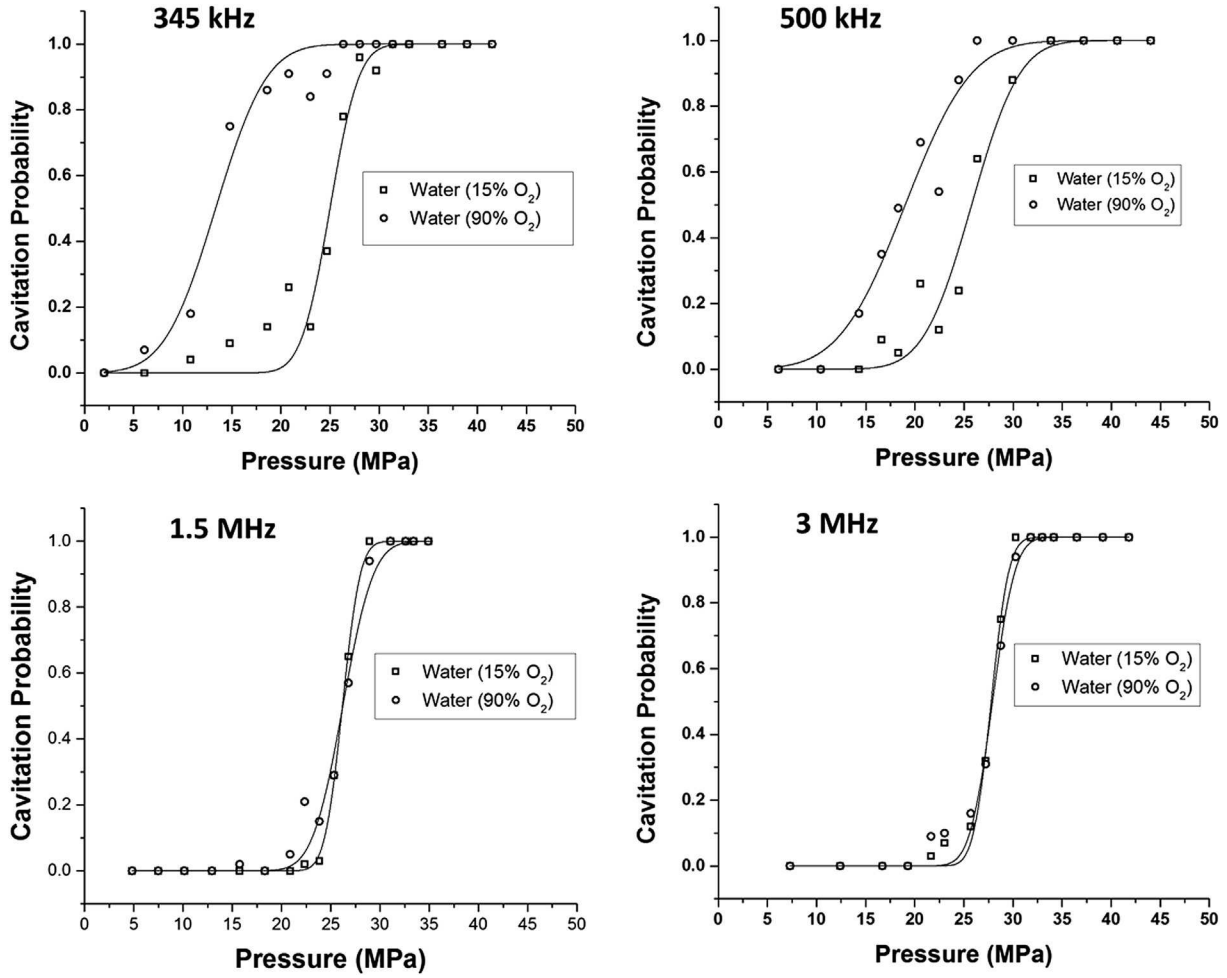

Fig. 5. Cavitation threshold in water. Example probability curves for water samples. Results revealed a significant decrease in the cavitation threshold for 90% O_2 water at 345 and 500 kHz, compared with degassed 15% O_2 water. No significant difference was observed between 90% O_2 and 15% O_2 water at 1.5 or 3 MHz.

RESULTS

Intrinsic threshold in water

To investigate the effects of ultrasound frequency on the intrinsic threshold, histotripsy pulses were first applied to distilled, degassed water using the 345-kHz, 500-kHz, 1.5-MHz and 3-MHz histotripsy transducers. Optical imaging results indicate that the intrinsic threshold, p_{int}, in water was found to be in the ranges p_{int} = 24.9–27.7 MPa, with σ_{mean} = 1.6 MPa for 345 kHz; p_{int} = 25.8–26.7 MPa, with σ_{mean} = 2 MPa for 500 kHz; p_{int} = 26.2–27.8 MPa, with σ_{mean} = 1.2 MPa for 1.5 MHz; and p_{int} = 26.1–27.9 MPa, with σ_{mean} = 1.1 MPa for 3 MHz. In Figure 3 are example images taken using the 1.5-MHz transducer at peak negative-pressure levels from below to above the intrinsic threshold. In the experimental data for all frequencies, cavitation was observed with p_{cav} = 1 for p_- >30 MPa. As pressure was increased above the intrinsic threshold, the bubbles were visualized in an increasingly larger area with a greater number of bubbles present in this focal region, as has been previously observed (Lin et al. 2014c; Maxwell et al. 2013). Although the bubbles covered a larger area at higher pressure, the diameter of bubbles that could be individually identified appeared to be consistent between pressure levels for the same frequency at the time point captured by the camera, potentially because of bubble–bubble interactions suppressing the growth of adjacent bubbles or bubble-induced pressure saturation caused by energy loss into each bubble as it forms, which has previously been observed in shock wave lithotripsy (Freund 2008; Pishchalnikov et al. 2008). When frequency was varied, differences in bubble size were noted, with lower frequency producing larger bubbles.

In addition to high-speed imaging, cavitation was monitored using one of the therapy transducer elements

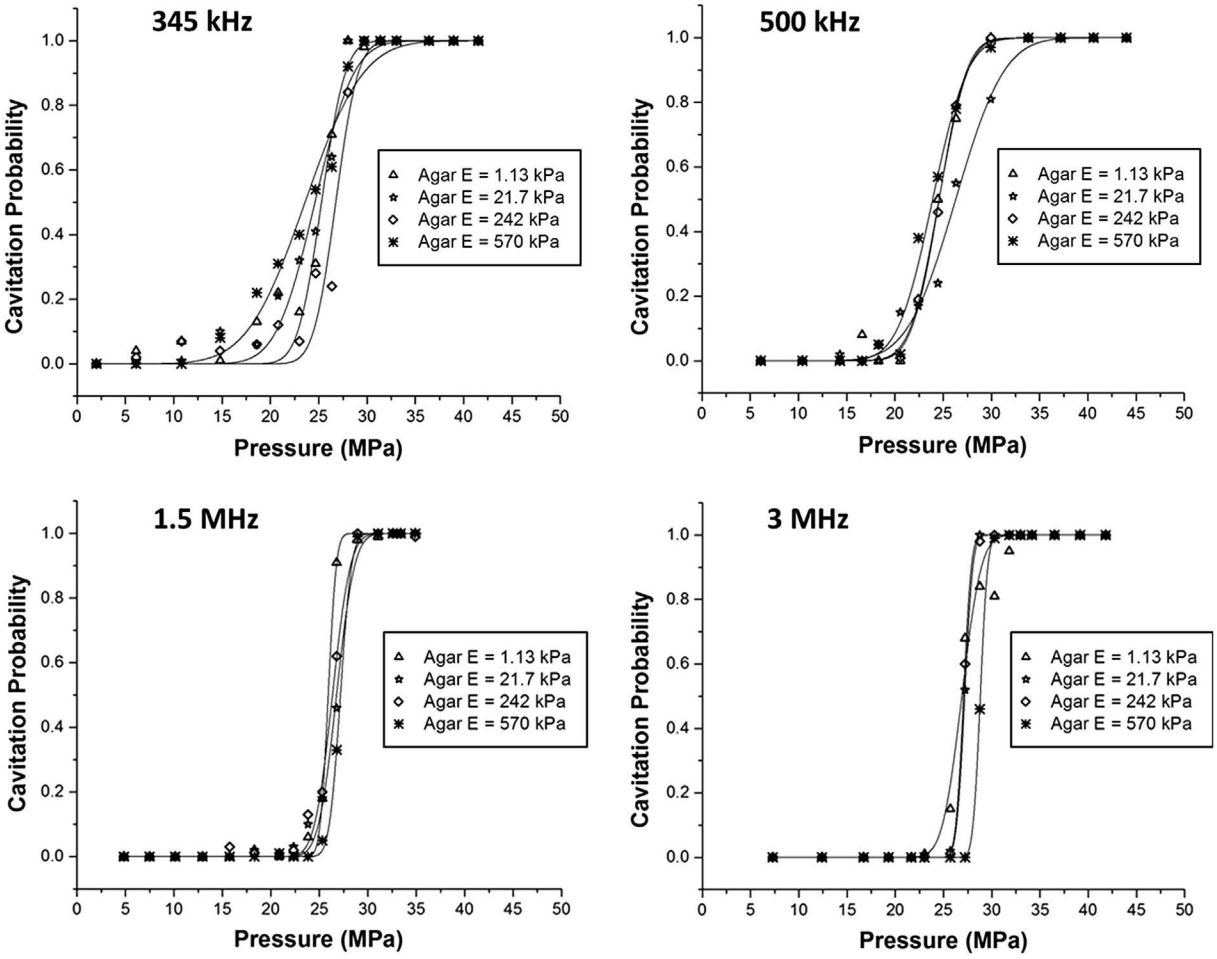

Fig. 6. Cavitation threshold in tissue phantoms. Example probability curves for mechanically tunable agarose tissue phantoms. Results indicated no significant difference in the intrinsic threshold with increasing stiffness. A small increase of ~2–3 MPa was observed in the threshold as the frequency was increased from 345 kHz to 3 MHz.

for PCD according to a previously established method (Maxwell et al. 2013). The cavitation detection results from PCD and optical imaging methods matched well in water (Fig. 3). When cavitation occurred on high-speed images, the PCD signal was a multicycle burst of significantly increased amplitude with a center frequency near the therapy transducer frequency. When no cavitation was observed on the camera, the PCD signal amplitude was small. Figure 4 illustrates an example of the relative values of S_{PCD} versus pulse number for 100 pulses near the intrinsic threshold in degassed water using the 1.5-MHz transducer.

The gas concentration of the water sample had a small effect on the cavitation probability curve at 1.5 and 3 MHz, but caused a large difference at 345 and 500 kHz (Fig. 5). For example, the cavitation threshold in both degassed (15% O_2) and gassy (90% O_2) water was between 26.3 and 27.4 MPa for all samples at 1.5 and 3 MHz. In contrast, the cavitation threshold in gassy water (90% O_2) was observed to decrease by 6.5 MPa at 500 kHz and 13.6 MPa at 345 kHz compared with the intrinsic threshold in degassed water (15% O_2) (Fig. 5).

Intrinsic threshold in tissue phantoms

To investigate the effects of tissue stiffness on the intrinsic threshold, experiments were repeated inside mechanically tunable tissue phantoms. Four types of tissue phantoms were tested at each frequency, with the Young's moduli ranging from 1.13 to 570 kPa. Results revealed a similar function of cavitation probability versus pressure in all tissue phantoms (Fig. 6). Furthermore, the intrinsic threshold was observed to be similar in tissue phantoms of all Young's moduli. For example, at 1.5 MHz, the intrinsic threshold for the four types of tissue phantoms ranged from 24.8 to 26.7 MPa (Table 2). The region over which cavitation occurred in each sample was similar at similar pressure levels. One difference between tissue phantoms was that the bubbles observed in stiffer tissue phantoms were smaller in size at the time point captured by the camera (Fig. 7).

Table 2. Threshold results: All samples*

Frequency	Material	p_{int} (1)	p_{int} (2)	p_{int} (3)	p_{int} (Mean)	σ (mean)
345 kHz	Water (15% O_2)	27.7	24.9	25.0	25.9	1.6
	Water (90% O_2)	10.7	13.3	12.8	12.3	3.8
	Agar E = 1.13 kPa	25.8	23.7	24.6	24.7	2.0
	Agar E = 21.7 kPa	25.9	23.7	24.7	24.8	2.0
	Agar E = 242 kPa	26.8	24.8	25.0	25.5	1.9
	Agar E = 570 kPa	25.9	24.9	23.6	24.8	2.2
	Liver	24.9	25.5	24.0	24.8	1.9
	Tongue	25.0	25.6	26.5	25.7	1.4
	Tendon	27.8	27.7	27.4	27.6	1.4
500 kHz	Water (15% O_2)	25.9	25.8	26.7	26.1	2.0
	Water (90% O_2)	20.3	19.0	19.6	19.6	3.6
	Agar E = 1.13 kPa	24.6	23.5	27.6	25.2	1.8
	Agar E = 21.7 kPa	23.5	26.3	26.7	25.5	1.8
	Agar E = 242 kPa	24.6	26.9	24.9	25.5	2.0
	Agar E = 570 kPa	24.7	26.3	23.9	25.0	1.8
	Liver	25.1	26.5	24.3	25.3	2.0
	Tongue	25.0	25.6	25.0	25.2	2.2
	Tendon	28.1	28.9	27.7	28.2	2.8
1.5 MHz	Water (15% O_2)	27.6	27.8	26.2	27.2	1.2
	Water (90% O_2)	26.2	26.9	25.7	26.3	1.6
	Agar E = 1.13 kPa	25.9	25.5	27.9	26.4	0.7
	Agar E = 21.7 kPa	26.8	27.0	26.3	26.7	1.0
	Agar E = 242 kPa	27.2	25.9	26.7	26.6	0.7
	Agar E = 570 kPa	25.7	23.8	24.9	24.8	0.7
	Liver	27.0	26.7	28.8	27.5	1.5
	Tongue	28.2	26.8	28.1	27.7	1.4
	Tendon	28.8	29.9	28.6	29.1	1.6
3 MHz	Water (15% O_2)	27.8	27.9	26.1	27.3	1.1
	Water (90% O_2)	27.1	27.2	27.9	27.4	1.1
	Agar E = 1.13 kPa	28.4	26.9	27.1	27.5	1.3
	Agar E = 21.7 kPa	26.9	27.2	26.3	26.8	0.9
	Agar E = 242 kPa	27.1	26.6	27.0	26.9	0.8
	Agar E = 570 kPa	27.4	28.8	27.2	27.8	0.7
	Liver	27.4	26.5	27.6	27.2	1.1
	Tongue	28.5	28.1	28.7	28.5	1.2
	Tendon	30.3	31.5	30.1	30.6	0.8

* All values are pressures in MPa. Statistical analysis revealed that for all sample types, a pair of samples existed within one sample type with a statistically significant difference ($p < 0.05$). Additionally, there existed at least one pair in any two sample types with a significant difference.

The PCD was found to remain sensitive to the cavitation bubbles formed in all tissue phantoms despite the differences in bubble size (Fig. 7). Comparison of the effects of frequency on the threshold in tissue phantoms revealed a small difference of ~2–3 MPa in the intrinsic threshold when the frequency was increased from 345 kHz to 3 MHz. The average intrinsic threshold for all phantom and frequency combinations ranged from 24.7 to 27.8 MPa (Table 2).

Intrinsic threshold in bovine tissue

To validate the results from water and tissue phantom experiments, the intrinsic threshold was investigated in select *ex vivo* bovine tissues. Bovine liver (E = 8.7 kPa), tongue (E = 25 kPa), and tendon (E = 380 MPa) were chosen to cover a wide range of tissue strength. In these tissues, PCD detection had a function of cavitation probability versus pressure in tissues similar to those in tissue phantoms and degassed water (Fig. 8). The intrinsic threshold was observed to be similar in all tissues, with only a small increase observed for tendon (Fig. 8). For example, at 1.5 MHz, the average intrinsic threshold for the three types of tissue ranged from 27.5 MPa (liver) to 29.1 MPa (tendon). Comparison of the effects of frequency on the intrinsic threshold revealed a small increase with increasing frequency. For example, in liver samples, the intrinsic threshold ranged from 24.8 MPa at 345 kHz to 27.2 MPa at 3 MHz. The intrinsic threshold for all tissues and frequency combinations ranged from 24.8 to 30.6 MPa.

Intrinsic threshold comparison

The intrinsic thresholds of all samples were compared using the curve-fitting method and statistical analysis described above. In general, the standard errors in the estimate of the intrinsic threshold, p_{int}, were small compared with the variance between samples of the same type. Excluding the gassy water (90% O_2), p_{int} for all samples and frequencies was observed to be between 24.8 and 30.6 MPa, and the σ_{mean} between 0.7 and 2.8 MPa. The full cavitation threshold results for all samples are listed in Table 2. Overall, results revealed no noticeable trend in the intrinsic threshold between samples with Young's moduli <1 MPa. However, a small increase of ~2–3 MPa was observed for tendon (E = 380 MPa) compared with other samples (E = 1.13–570 kPa). Additionally, results revealed a small but consistent increase in the intrinsic threshold of ~2–3 MPa when the frequency was increased from 345 kHz to 3 MHz (Fig. 9a). It should be noted that in addition to the small changes in threshold observed with changes in frequency, larger σ_{mean} values were observed at 345 and 500 kHz than at 1.5 and 3 MHz (Table 2).

A two-way analysis of variance performed on the data illustrated in Figure 9a revealed no significant difference in the threshold between samples at a given frequency, with the exception of the threshold in tendon, which was observed to be significantly increased ($p <$ 0.05). The analysis of variance also revealed a significant increase in the threshold between 345 kHz and 3 MHz for all samples. However, only some of the differences between intermediate frequencies were significant. The effects of Young's modulus and ultrasound frequency were also analyzed by plotting p_{int} for all samples except 90% O_2 water (Table 2) as a function of Young's modulus and frequency (Fig. 9). Linear regression analysis revealed that the change in p_{int} with increasing Young's modulus (tendon not included) was not significant *via* the Pearson correlation ($r = -0.173$, $R^2 = 0.03$, $p > 0.05$) (Fig. 9b), but the change in p_{int} with increasing frequency was significant *via* the Pearson correlation ($r = 0.57$, $R^2 = 0.32$, $p < 0.05$) (Fig. 9c).

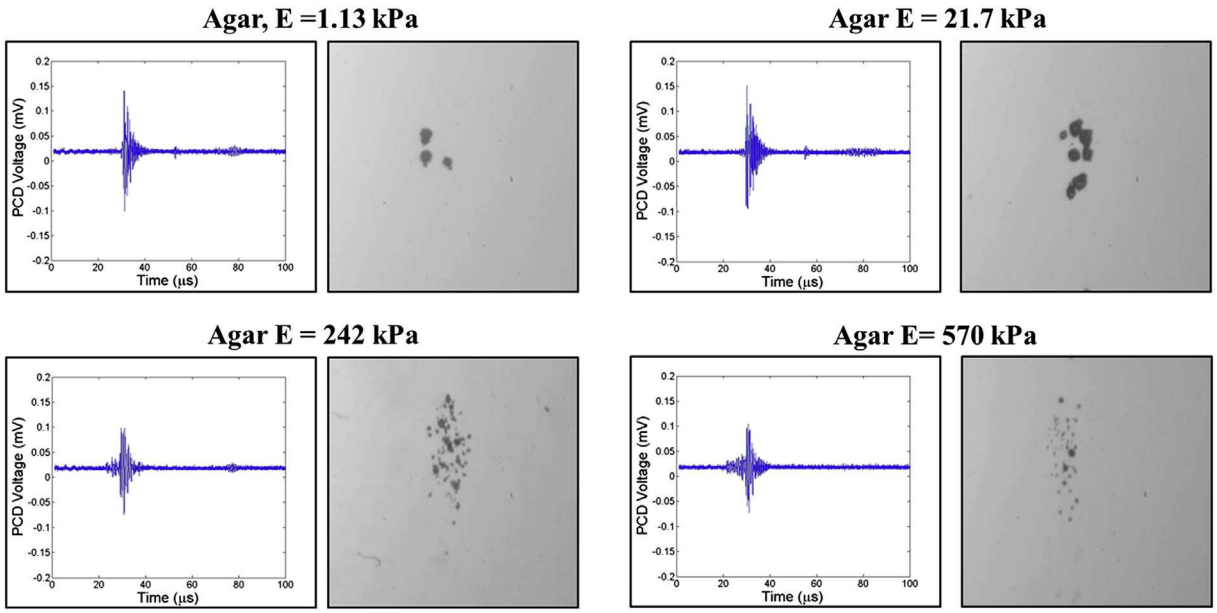

Fig. 7. Cavitation detection in tissue phantoms. Example passive cavitation detection (PCD) signals (left) and corresponding optical images (right) of cavitation in agarose tissue phantoms of increasing Young's moduli. The PCD signal was observed to remain sensitive to cavitation in stiffer phantoms despite the observe decrease in bubble size.

Threshold simulation: Stabilized nuclei

To provide a theoretical explanation of the experimental results, the effects of tissue stiffness and ultrasound frequency on the cavitation threshold were investigated using a single-bubble numerical simulation assuming a nanometer-sized stable nucleus. When the peak negative pressure, p_A, was less than some threshold value, p_{t_sim}, bubble expansion was minimal ($R_{max} < 2R_0$). As p_A was increased above p_{t_sim}, great bubble growth and collapse were observed ($R_{max} > 10^4 R_0$). The peak negative pressure corresponding to this transition was defined as the inertial cavitation threshold, p_{t_sim}. By use of a 2.5-nm initial bubble, p_{t_sim} was observed to be ~28 MPa for all frequencies tested (Fig. 10a). Similarly, p_{t_sim} was observed to be independent of tissue elastic modulus from 1 kPa to ~1 MPa, because the threshold was dominated by surface tension rather than the macroscopic properties of the media such as the Young's modulus (Fig. 10b). However, when the Young's modulus was increased to 10 MPa, cavitation threshold was no longer determined solely by surface tension and p_{t_sim} increased to ~32 MPa (Fig. 10b). It should be noted that the simulation could not accurately predict the intrinsic threshold in tendon (E = 380 MPa). In contrast to the ~2- to 3-MPa increase in threshold observed experimentally, the model predicted a threshold of >315 MPa when the Young's modulus was 380 MPa.

The effects of initial size of the nuclei on the inertial cavitation threshold were also investigated, and a significant drop in the inertial cavitation threshold with increasing initial bubble radius was observed (Fig. 10). Simulations revealed that the experimentally observed thresholds corresponded to an initial bubble size between 2.3 nm (p_{t_sim} = 30.6 MPa) and 2.85 nm (p_{t_sim} = 24.7 MPa) (Fig. 10c). Simulations comparing a larger range of sizes of initial nuclei indicated a significant reduction in p_{t_sim} as the size of nuclei was increased from 2 nm to ~40–60 nm, at which point the threshold appeared to plateau (Fig. 10d). In the case of nuclei larger than ~40–60 nm, the final bubble size was dictated by several competing terms including the applied pressure and the tissue elasticity, rather than being dominated by surface tension as is the case for smaller initial bubbles, which led to bubbles expanding to approximately the same size with the same p_{t_sim} regardless of initial radius. This effect has also been observed in previous studies on shock wave lithotripsy (Zhong et al. 1998). The finding that the threshold decreased with increasing bubble radius, especially at lower frequency (Fig. 10d), helps to explain the significant decrease in cavitation for 90% O_2 water at 345 and 500 kHz (Fig. 5). However, it should also be noted that the likelihood of getting a large bubble in the field is much greater at low frequency than high frequency because of the larger focal volume (greater than two orders of magnitude difference between 345 kHz and 3 MHz), which was not accounted for in the single-bubble simulation and likely contributed to the experimental results.

Threshold simulation: Spontaneous nucleation

The effects of ultrasound frequency on the cavitation threshold predicted by CNT were also investigated with a simulation, as described under Methods (eqn 7). CNT

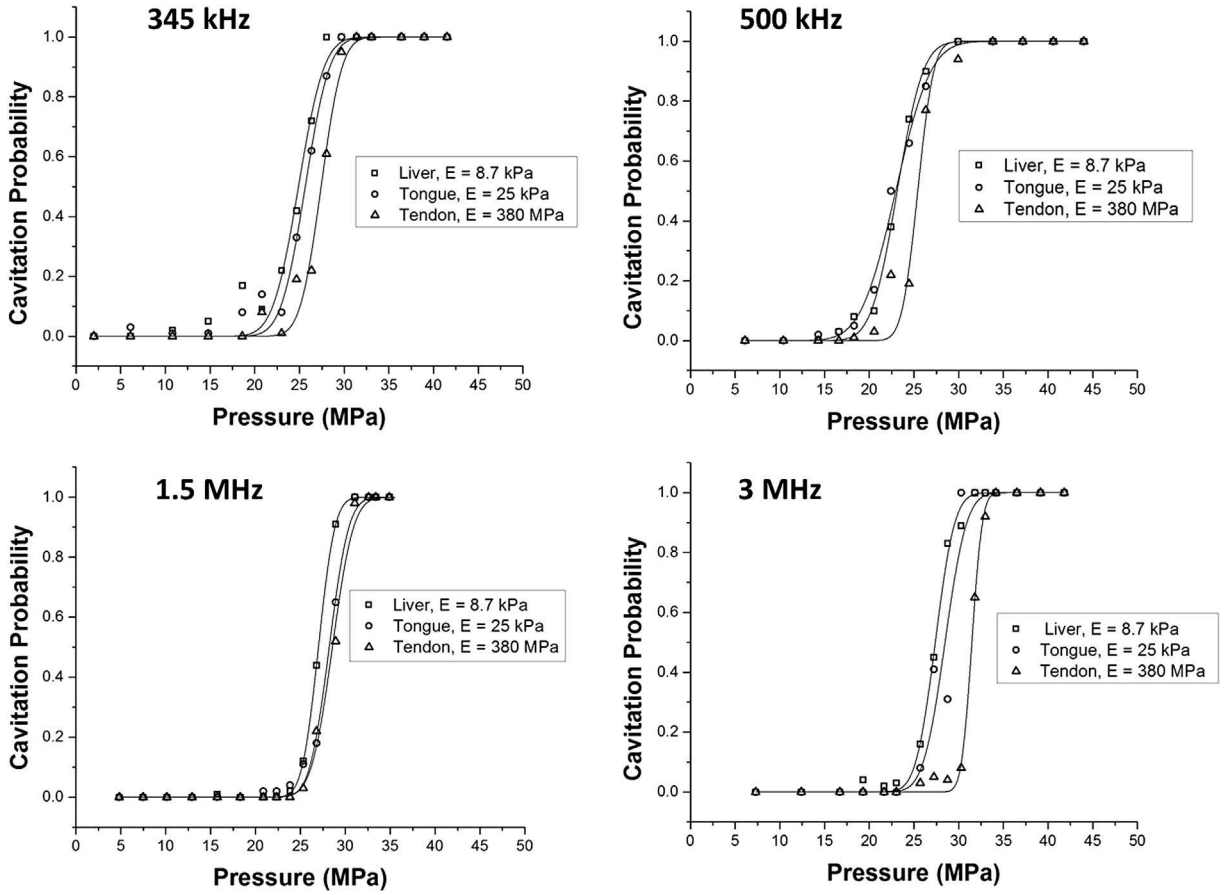

Fig. 8. Cavitation threshold in *ex vivo* bovine tissue. Example probability curves for *ex vivo* bovine liver, tongue, and tendon. A small increase of ~2–3 MPa was observed in the threshold as the frequency was increased from 345 kHz to 3 MHz.

results predicted that the cavitation threshold would increase by ~2.3 MPa when the frequency was increased from 345 kHz to 3 MHz. These results closely matched experiments, with the value of p_{t_CNT} increasing from 24.9 to 27.2 MPa when the frequency was increased from 345 kHz to 3 MHz (Fig. 11). Figure 11 illustrates p_{t_CNT} compared with the average p_{int} measured for all agarose tissue phantoms at each frequency. These results suggest that the increase in threshold at higher frequency measured experimentally is due to the smaller focal zone and shorter duration of the applied p_-. In fact, because bubbles are generated directly from the single p_- phase of the incident wave, it may be more appropriate to use the duration of the applied p_- as a metric instead of frequency, which may incorrectly imply periodic forcing.

DISCUSSION

In previous studies, stiffer tissues had increased resistance to histotripsy fractionation and required a higher pressure threshold to generate a cavitation cloud *via* the shock scattering method (Vlaisavljevich et al. 2014a, 2014b). In this study, the effects of tissue stiffness on the histotripsy intrinsic threshold were investigated, with results supporting our hypothesis that the intrinsic threshold is independent of tissue stiffness. At all frequencies tested, no noticeable trend of increasing threshold was observed for phantoms and tissues with Young's moduli <1 MPa, and only a small increase was observed for tendon (E = 380 MPa). The observed increase for tendon was also small (~2–3 MPa) in comparison to previously measured differences between water-based and non-water-based media such as 1,3-butanediol and adipose tissue, which resulted in a ~5- to 10-MPa change in the intrinsic threshold (Maxwell et al. 2013).

The finding that the intrinsic threshold is independent of tissue stiffness is of significant importance to the development of histotripsy therapy. As suggested by Maxwell and co-workers, the intrinsic threshold approach has the potential to create a more predictive and reliable histotripsy therapy (Lin et al. 2014c; Maxwell et al. 2013). In this study, we report that by using the intrinsic threshold method, histotripsy bubbles

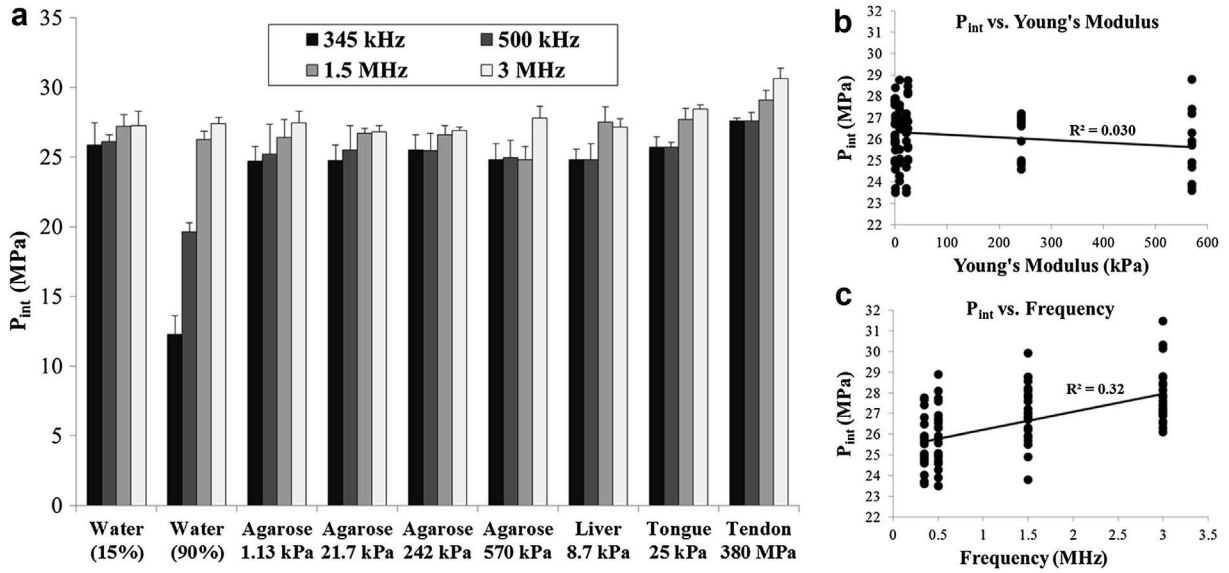

Fig. 9. Intrinsic threshold comparison. (a) Bar plot illustrates the p_{int} values measured for all samples and frequencies studied in this work. The threshold for all samples remained between 24.7 and 30.6 MPa with the exception of that for 90% O_2 water at 345 and 500 kHz, which was signficantly lower. Results revealed no trend in the intrinsic threshold with increasing stiffness for $E < 1$ MPa, but a small increase of ~2–3 MPa was observed for tendon ($E = 380$ MPa). (b) Linear regression analysis revealed that the change in p_{int} with increasing Young's modulus (tendon not included) was not significant *via* the Pearson correlation ($r = -0.173$, $R^2 = 0.030$, $p > 0.05$). (c) Linear regression analysis further revealed that the ~2- to 3-MPa increase in p_{int} with increasing frequency was significant *via* the Pearson correlation ($r = 0.57$, $R^2 = 0.32$, $p < 0.05$).

can be reliably generated at the same pressure in many tissue types. As a result, initiating cavitation above the intrinsic threshold appears to be much more predictable than using shock scattering, which has been found to require higher pressure to generate a bubble cloud in stiffer tissues (Vlaisavljevich et al. 2014b). For the same reasons, the intrinsic threshold approach is also more predictable and reproducible than cavitation initiation using longer pulses or adding contrast agents, even though these methods can lower cavitation threshold (Carstensen et al. 2000; Fowlkes and Crum 1988; Holland and Apfel 1990; Kyriakou et al. 2011; Miller and Thomas 1995). It should, however, be noted that stiffer tissues may remain resistant to histotripsy fractionation even in cases when a bubble cloud has been generated, because of impeded bubble expansion as well as the higher ultimate stress and ultimate strain of these tissues (Vlaisavljevich et al. 2013b, 2014a, 2015). It is likely that the decrease in bubble expansion in stiffer tissues, which were observed in this study, will result in a decrease in the rate and extent of tissue fractionation, even in cases when a bubble cloud has been initiated. As a result, use of a lower frequency may be necessary to facilitate bubble expansion for the treatment of stiffer tissues.

In addition to tissue stiffness, this work investigated the effects of frequency on the intrinsic threshold, with the results indicating a small increase of ~2–3 MPa when the frequency was increased from 345 kHz to 3 MHz, which covers the range frequently used for histotripsy therapy. Because the intrinsic threshold was observed to be nearly independent of frequency for the histotripsy therapy range, treatment optimization strategies can instead focus on other considerations such as the desired bubble expansion, the optimal focal zone or the available acoustic window required for the treatment of specific tissues. For example, the larger focal zone at lower frequency may be used in instances when large volume ablation is desired, such as the removal of large tumors in the liver (Vlaisavljevich et al. 2013b). On the other hand, higher frequency may provide a smaller focal zone for treatments in which high precision is required, such as the removal of blood clots in deep-vein thrombosis or stroke (Maxwell et al. 2009).

Another observation that may help guide histotripsy parameter optimization is the finding that "incidental cavitation bubbles" formed below the intrinsic threshold are more likely to be generated at lower frequency, which was observed in 90% O_2 water at 345 and 500 kHz (Fig. 5). This finding suggests that using a higher frequency will reduce the risk of collateral damage outside the treatment region by minimizing "incidental bubbles" formed in these external locations, which was previously observed in a study comparing histotripsy fractionation at 500 kHz and 3 MHz (Lin et al. 2014a). Additionally, this finding suggests that lower frequency may enhance the

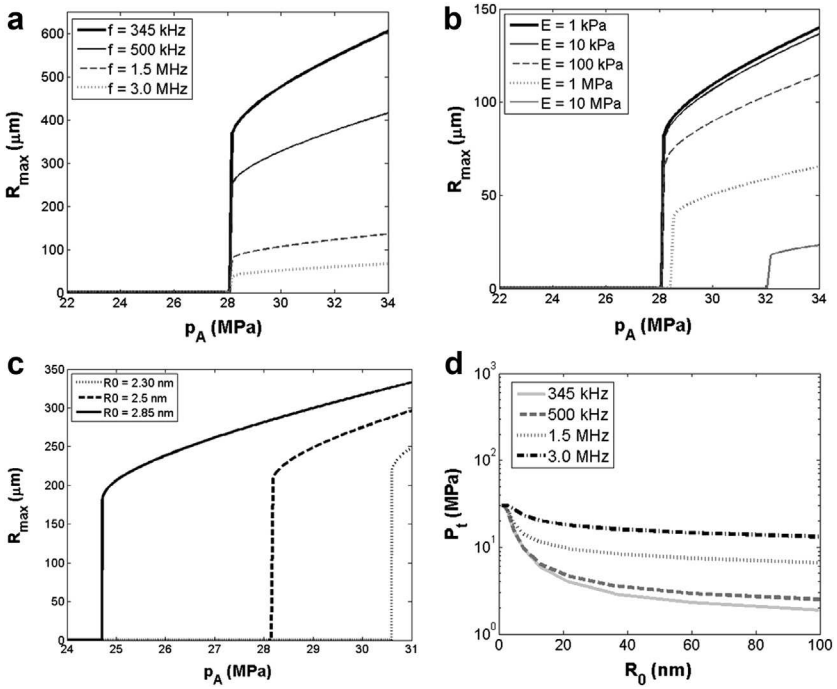

Fig. 10. Stabilized Nuclei Simulation. Simulated maximum bubble radius for a 2.5-nm initial bubble subjected to a single-cycle histotripsy peak negative-pressure waveform revealed a distinct threshold of ~28 MPa that was independent of (a) ultrasound frequency (E = 1 kPa) and (b) tissue stiffness for Young's moduli <1 MPa (f = 1.5 MHz). (c) Simulations indicated that the cavitation threshold measured experimentally (24.7–30.6 MPa) corresponded to initial bubble sizes between 2.3 and 2.85 nm (E = 1 kPa, f = 500 kHz). (d) Increasing the initial bubble size from 1 to 100 nm resulted in a decrease in the cavitation threshold, with a larger decrease observed at lower frequency (E = 1 kPa).

shock scattering process, which relies on cavitation generation from incidental bubbles and the expansion of these initial bubbles, both of which were enhanced at lower frequency in this study.

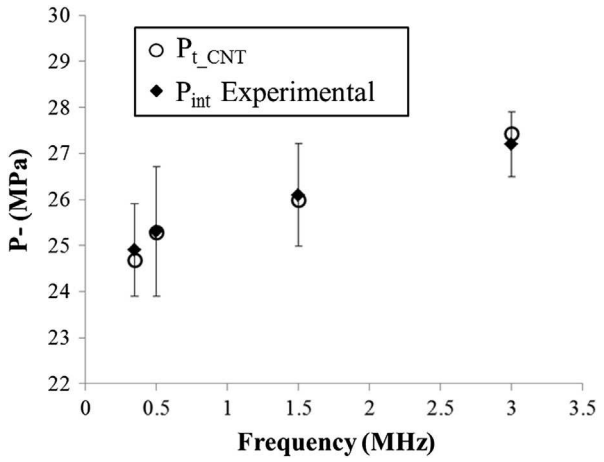

Fig. 11. Classic nucleation theory (CNT) simulation. Classic nucleation theory was used to predict the effects of frequency on the cavitation threshold using eqn (7). Results revealed an increase in p_{t_CNT} of 2.7 MPa as the frequency was increased from 345 kHz to 3 MHz (o). Comparisons with the average experimental results for p_{int} in agarose tissue phantoms (◆) indicated close agreement between theory and experiments.

In the final part of this study, two models were used to provide some insight into the "intrinsic nuclei" population. First, a stable bubble model was used, predicting a threshold that was independent of tissue stiffness for Young's moduli <1 MPa. However, the model was inaccurate for Young's moduli >1 MPa and could not accurately predict the threshold in tendon. This result, along with the experimental observation that the intrinsic threshold in tissue is similar to the intrinsic threshold in water, suggests that nucleation actually occurs in the water inside tissue, where the Young's modulus is negligible. If this is true, the Young's modulus would affect only macroscopic bubble motion, but not the initial bubble behavior. This would explain why the model is inaccurate for large Young's moduli; it models homogeneous bulk tissue properties down to very small sizes that do not reflect actual tissue conditions at the nanoscopic scale (*i.e.,* porosity, anisotropy). The stable bubble model further indicated that the cavitation threshold was independent of frequency for the range tested for a 2.5-nm initial bubble and predicted that the thresholds measured in experiments (24.7–30.6 MPa) corresponded to initial bubble sizes between 2.3 and 2.85 nm. Although this analysis may shed some light on the possible size range of stable nuclei in tissue, it is unlikely that the changes in threshold with frequency are due to changes in the

size of nuclei, as the same samples were exposed for all frequencies. It is more likely that the decrease in threshold at lower frequency is due to the larger focal volume and increased duration of the applied pressure, as predicted by the CNT model. The change in threshold predicted by CNT closely matched experimental results in the present study, as well as the results of Arvengas et al. (2011a), who measured the cavitation probability between 1 and 2 MHz. Comparison of the effects of frequency predicted by CNT and the stable bubble model suggests that the intrinsic threshold generates bubbles from spontaneous nuclei within the water inside tissue. However, although these results provide some insight into the potential intrinsic nuclei population, future work is required to conclusively determine whether the intrinsic nuclei are actually spontaneous nuclei described by classic nucleation theory or nanometer-sized stabilized gas nuclei, or if a more advanced microscopic model is needed to describe these nuclei.

CONCLUSIONS

In this study, the effects of tissue stiffness and ultrasound frequency on the histotripsy intrinsic threshold were investigated by applying 1- to 2-cycle histotripsy pulses to mechanically tunable tissue phantoms and *ex vivo* bovine tissues using 345-kHz, 500-kHz, 1.5-MHz and 3-MHz histotripsy transducers. Results revealed that the histotripsy intrinsic threshold is independent of stiffness for tissue phantoms and soft tissues with Young's moduli <1 MPa, with only a small increase in the intrinsic threshold observed for tendon ($E = 380$ MPa). Results further revealed only a small increase in the intrinsic threshold of $\sim$2–3 MPa when the frequency was increased from 345 kHz to 3 MHz. Overall, the results of this study suggest that the intrinsic threshold approach is predictable and reproducible in initiating cavitation, regardless of the tissue type and frequency used.

Acknowledgments—Eli Vlaisavljevich was supported by a National Science Foundation Graduate Research Fellowship. This work was supported by grants from the National Institute of Biomedical Imaging and Bioengineering (NIBIB) of the National Institutes of Health under Award R01 EB008998; a Research Scholar Grant from the American Cancer Society (RSG-13-101-01-CCE); a National Science Foundation Grant (CBET 1253157); The Hartwell Foundation; and the Focused Ultrasound Foundation.

REFERENCES

Arvengas A, Davitt K, Caupin F. Fiber optic probe hydrophone for the study of acoustic cavitation in water. Rev Sci Instrum 2011a;82:034904.

Arvengas A, Herbert E, Cersoy S, Davitt K, Caupin F. Cavitation in heavy water and other liquids. J Phys Chem B 2011b;115:14240–14245.

Balgude AP, Yu X, Szymanski A, Bellamkonda RV. Agarose gel stiffness determines rate of DRG neurite extension in 3-D cultures. Biomaterials 2001;22:1077–1084.

Blake FG. Gas bubbles as cavitation nuclei. Phys Rev 1949;75:1313.

Briggs LJ. The limiting negative pressure of water. J Appl Phys 1950;21:721–722.

Bunkin NF, Suyazov NV, Shkirin AV, Ignat'ev PS, Indukaev KV. Cluster structure of stable dissolved gas nanobubbles in highly purified water. J Exp Theor Phys 2009;108:800–816.

Carstensen EL, Gracewski S, Dalecki D. The search for cavitation *in vivo*. Ultrasound Med Biol 2000;26:1377–1385.

Caupin F, Herbert E. Cavitation in water: A review. C R Phys 2006;7:1000–1017.

Diem K, Lentner C. Documenta Geigy scientific tables. 7th ed. London/New York: Wiley; 1970.

Duck FA. Physical properties of tissue: A comprehensive reference book. New York: Academic Press; 1990.

Fisher JC. The fracture of liquids. J Appl Phys 1948;19:1062–1067.

Fowlkes JB, Crum LA. Cavitation threshold measurements for microsecond length pulses of ultrasound. J Acoust Soc Am 1988;83:2190–2201.

Freund JB. Suppression of shocked-bubble expansion due to tissue confinement with application to shock-wave lithotripsy. J Acoust Soc Am 2008;123:2867–2874.

Greenspan M, Tschiegg CE. Radiation-induced acoustic cavitation: Threshold versus temperature for some liquids. J Acoust Soc Am 1982;72:1327–1331.

Hall TL, Kieran K, Ives K, Fowlkes JB, Cain CA, Roberts WW. Histotripsy of rabbit renal tissue *in vivo*: Temporal histologic trends. J Endourol 2007;21:1159–1166.

Harvey EN, Barnes DK, McElroy WD, Whiteley AH, Pease DC, Cooper KW. Bubble formation in animals: I. Physical factors. J Cell Comp Physiol 1944;24:1–22.

Herbert E, Balibar S, Caupin F. Cavitation pressure in water. Phys Rev E 2006;74(4, Pt 1):041603.

Holland CK, Apfel RE. Thresholds for transient cavitation produced by pulsed ultrasound in a controlled nuclei environment. J Acoust Soc Am 1990;88:2059–2069.

Hosmer DW, Lemeshow S. Confidence interval estimation of interaction. Epidemiology 1992;3:452–456.

International Commission on Radiological Protection (ICRP). Report of the Task Group on Reference Man: A report. Oxford/New York: Pergamon Press; 1975.

International Commission on Radiation Units and Measurements (ICRU). Tissue substitutes in radiation dosimetry and measurement. Report 44. Bethesda, MD: Author; 1989.

Keller JB, Miksis M. Bubble oscillations of large-amplitude. J Acoust Soc Am 1980;68:628–633.

Kyriakou Z, Corral-Baques MI, Amat A, Coussios CC. HIFU-induced cavitation and heating in *ex vivo* porcine subcutaneous fat. Ultrasound Med Biol 2011;37:568–579.

Leighton TG. The acoustic bubble. San Diego: Academic Press; 1994.

Lin KW, Duryea AP, Kim Y, Hall TL, Xu Z, Cain CA. Dual-beam histotripsy: a low-frequency pump enabling a high-frequency probe for precise lesion formation. IEEE Trans Ultrason Ferroelectr Freq Control 2014a;61:325–340.

Lin KW, Hall TL, McGough RJ, Xu Z, Cain CA. Synthesis of monopolar ultrasound pulses for therapy: The frequency-compounding transducer. IEEE Trans Ultrason Ferroelectr Freq Control 2014b;61:1123–1136.

Lin KW, Kim Y, Maxwell AD, Wang TY, Hall TL, Xu Z, Fowlkes JB, Cain CA. Histotripsy beyond the intrinsic cavitation threshold using very short ultrasound pulses: Microtripsy. IEEE Trans Ultrason Ferroelectr Freq Control 2014c;61:251–265.

Maxwell AD, Cain CA, Duryea AP, Yuan L, Gurm HS, Xu Z. Noninvasive thrombolysis using pulsed ultrasound cavitation therapy—Histotripsy. Ultrasound Med Biol 2009;35:1982–1994.

Maxwell AD, Cain CA, Fowlkes JB, Xu Z. Inception of cavitation clouds by scattered shockwaves. Proc IEEE Ultrason Symp 2010;108–111.

Maxwell AD, Cain CA, Hall TL, Fowlkes JB, Xu Z. Probability of cavitation for single ultrasound pulses applied to tissues and tissue-mimicking materials. Ultrasound Med Biol 2013;39:449–465.

Maxwell AD, Wang TY, Cain CA, Fowlkes JB, Sapozhnikov OA, Bailey MR, Xu Z. Cavitation clouds created by shock scattering from bubbles during histotripsy. J Acoust Soc Am 2011a;130: 1888–1898.

Maxwell AD, Wang TY, Cain CA, Fowlkes JB, Sapozhnikov OA, Bailey MR, Xu Z. Cavitation clouds created by shock scattering from bubbles during histotripsy. J Acoust Soc Am 2011b;130: 1888–1898.

Miller DL, Thomas RM. Ultrasound contrast agents nucleate inertial cavitation in-vitro. Ultrasound Med Biol 1995;21:1059–1065.

Parsons JE, Cain CA, Abrams GD, Fowlkes JB. Pulsed cavitational ultrasound therapy for controlled tissue homogenization. Ultrasound Med Biol 2006a;32:115–129.

Parsons JE, Cain CA, Fowlkes JB. Cost-effective assembly of a basic fiber-optic hydrophone for measurement of high-amplitude therapeutic ultrasound fields. J Acoust Soc Am 2006b;119:1432–1440.

Parsons JE, Cain CA, Fowlkes JB. Spatial variability in acoustic backscatter as an indicator of tissue homogenate production in pulsed cavitational ultrasound therapy. IEEE Trans Ultrason Ferroelectr Freq Control 2007;54:576–590.

Pettersen MS, Balibar S, Maris HJ. Experimental investigation of cavitation in superfluid 4 He. Phys Rev B Condens Matter 1994;49: 12062–12070.

Pishchalnikov YA, McAteer JA, Williams JC Jr. Effect of firing rate on the performance of shock wave lithotriptors. BJU Int 2008;102: 1681–1686.

Roberts WW, Hall TL, Ives K, Wolf JS Jr, Fowlkes JB, Cain CA. Pulsed cavitational ultrasound: a non-invasive technology for controlled tissue ablation (histotripsy) in the rabbit kidney. J Urol 2006;175:734–738.

Roy RA, Madanshetty SI, Apfel RE. An acoustic backscattering technique for the detection of transient cavitation produced by microsecond pulses of ultrasound. J Acoust Soc Am 1990;87:2451–2458.

Sankin GN, Teslenko VS. Two-threshold cavitation regime. Dokl Phys 2003;48:665–668.

Staubli HU, Schatzmann L, Brunner P, Rincon L, Nolte LP. Mechanical tensile properties of the quadriceps tendon and patellar ligament in young adults. Am J Sports Med 1999;27:27–34.

Ulrich TA, Jain A, Tanner K, MacKay JL, Kumar S. Probing cellular mechanobiology in three-dimensional culture with collagen–agarose matrices. Biomaterials 2010;31:1875–1884.

Vlaisavljevich E, Durmaz YY, Maxwell A, Elsayed M, Xu Z. Nanodroplet-mediated histotripsy for image-guided targeted ultrasound cell ablation. Theranostics 2013a;3:851–864.

Vlaisavljevich E, Kim Y, Allen S, Owens G, Pelletier S, Cain C, Ives K, Xu Z. Image-guided non-invasive ultrasound liver ablation using histotripsy: Feasibility study in an *in vivo* porcine model. Ultrasound Med Biol 2013b;39:1398–1409.

Vlaisavljevich E, Kim Y, Owens G, Roberts W, Cain C, Xu Z. Effects of tissue mechanical properties on susceptibility to histotripsy-induced tissue damage. Phys Med Biol 2014a;59:253–270.

Vlaisavljevich E, Maxwell A, Warnez M, Johnsen E, Cain CA, Xu Z. Histotripsy-induced cavitation cloud initiation thresholds in tissues of different mechanical properties. IEEE Trans Ultrason Ferroelectr Freq Control 2014b;61:341–352.

Vlaisavljevich E, Lin KW, Warnez MT, Singh R, Mancia L, Putnam AJ, Johnsen E, Cain C, Xu Z. Effects of tissue stiffness, ultrasound frequency, and pressure on histotripsy-induced cavitation bubble behavior. Phys Med Biol 2015;60:2271–2292.

Woodard HQ, White DR. The composition of body tissues. Br J Radiol 1986;59:1209–1218.

Xu Z, Fowlkes JB, Rothman ED, Levin AM, Cain CA. Controlled ultrasound tissue erosion: The role of dynamic interaction between insonation and microbubble activity. J Acoust Soc Am 2005;117: 424–435.

Xu Z, Raghavan M, Hall TL, Chang CW, Mycek MA, Fowlkes JB, Cain CA. High speed imaging of bubble clouds generated in pulsed ultrasound cavitational therapy—Histotripsy. IEEE Trans Ultrason Ferroelectr Freq Control 2007;54:2091–2101.

Yamada H. Strength of biologic materials. New York: Robert E. Kreiger; 1973.

Yang X, Church CC. A model for the dynamics of gas bubbles in soft tissue. J Acoust Soc Am 2005;118:3595–3606.

Yount DE. Skins of varying permeability: Stabilization mechanism for gas cavitation nuclei. J Acoust Soc Am 1979;65: 1429–1439.

Zhong P, Cioanta I, Zhu SL, Cocks FH, Preminger GM. Effects of tissue constraint on shock wave-induced bubble expansion *in vivo*. J Acoust Soc Am 1998;104:3126–3129.